

Evolution of defect structures leading to high ZT in GeTe-based thermoelectric materials

Received: 21 July 2022

Accepted: 1 October 2022

Published online: 14 October 2022

 Check for updates

Yilin Jiang¹, Jinfeng Dong¹, Hua-Lu Zhuang¹, Jincheng Yu¹, Bin Su¹, Hezhang Li², Jun Pei¹, Fu-Hua Sun³, Min Zhou⁴, Haihua Hu¹, Jing-Wei Li¹, Zhanran Han¹, Bo-Ping Zhang⁵, Takao Mori^{2,6} & Jing-Feng Li^{1,3}

GeTe is a promising mid-temperature thermoelectric compound but inevitably contains excessive Ge vacancies hindering its performance maximization. This work reveals that significant enhancement in the dimensionless figure of merit (ZT) could be realized by defect structure engineering from point defects to line and plane defects of Ge vacancies. The evolved defects including dislocations and nanodomains enhance phonon scattering to reduce lattice thermal conductivity in GeTe. The accumulation of cationic vacancies toward the formation of dislocations and planar defects weakens the scattering against electronic carriers, securing the carrier mobility and power factor. This synergistic effect on electronic and thermal transport properties remarkably increases the quality factor. As a result, a maximum $ZT > 2.3$ at 648 K and a record-high average ZT (300–798 K) were obtained for $\text{Bi}_{0.07}\text{Ge}_{0.90}\text{Te}$ in lead-free GeTe-based compounds. This work demonstrates an important strategy for maximizing the thermoelectric performance of GeTe-based materials by engineering the defect structures, which could also be applied to other thermoelectric materials.

Thermoelectric technology has received increasing attention due to the capability of direct conversion from heat to electricity and vice versa. It can increase energy efficiency by harvesting waste heat for additional energy conversion^{1,2}, as well as other promising applications^{3,4}. The thermoelectric conversion efficiency can be evaluated by the dimensionless figure of merit (ZT) defined as $ZT = S^2\sigma T/\kappa$, where σ , S , T , and κ are the electrical conductivity, Seebeck coefficient, absolute temperature, and thermal conductivity, respectively. Here, κ can be mainly divided into electrical (κ_e) and lattice thermal conductivity (κ_L). Therefore, maximizing the power factor ($PF = S^2\sigma$) or minimizing κ_L is the basic rule for achieving high ZT values. Many methods have been utilized to improve PF ^{5,6} and suppress κ_L ^{7,8}.

Recently, a series of material systems with high ZT values have been reported, such as PbTe ^{9,10}, SnSe ^{11,12}, and Cu_2Se ¹³. It is acknowledged that PbTe -based materials are limited to special applications due to the general trend of pursuing environment-friendly materials. The latter two compounds possess high ZT at quite high temperatures, but show inferior performance at medium temperatures compared to PbTe -based materials.

GeTe, a non-toxic compound among the IV–VI families, is a p-type semiconductor with thermoelectric performance rivaling that of PbTe . GeTe possesses a less symmetrical rhombohedral structure (space group: $R\bar{3}m$), which enables the formation of ferroelectric domains, providing abundant microstructures^{14,15}. Recent advances in solid-state

¹State Key Laboratory of New Ceramics and Fine Processing, School of Materials Science and Engineering, Tsinghua University, Beijing 100084, China.

²International Center for Materials Nanoarchitectonics (WPI-MANA), National Institute for Materials Science (NIMS), Namiki 1-1, Tsukuba 305-0044, Japan. ³Institute for Advanced Materials, Hubei Normal University, Huangshi 435002, China. ⁴Key Laboratory of Cryogenics, Technical Institute of Physics and Chemistry, Chinese Academy of Sciences, Beijing 100190, China. ⁵The Beijing Municipal Key Laboratory of New Energy Materials and Technologies, School of Materials Science and Engineering, University of Science and Technology Beijing, Beijing 100083, China. ⁶Graduate School of Pure and Applied Sciences, University of Tsukuba, Tennoudai 1-1-1, Tsukuba 305-8671, Japan. ✉ e-mail: subin@tsinghua.edu.cn; mzhou@mail.ipc.ac.cn; MORI.Takao@nims.go.jp; jingfeng@mail.tsinghua.edu.cn

physics theories and material preparation techniques have provided various means of manipulating thermoelectric performance that prove to be effective. The symmetry-breaking and adjustable band structure provide more opportunities to manipulate and optimize the carrier transport properties^{16,17}. One of the conventional viewpoints is that PF can be effectively improved by modulating the symmetry and hence the band structure, which was manifested by the use of Pb^{18,19}, Cd²⁰, In^{21,22}, and Ti²³ as dopants. The lattice thermal conductivity was simultaneously suppressed by introducing point defects^{24,25}, stacking faults²⁶, and precipitates^{27,28}. High thermoelectric properties at medium temperatures were achieved in GeTe, rendering it an important compound with worldwide attention^{29–32}.

However, intrinsic Ge vacancies commonly exist in the stoichiometric GeTe, resulting in excessive holes, reaching a high concentration ($\sim 10^{21} \text{ cm}^{-3}$), which deviates far from the optimum value for thermoelectrics³³. On the other hand, the intrinsic vacancies impeding the carrier transport usually deteriorate the electrical properties. The dopants like Bi^{34,35}, Sb^{36,37}, and PbSe³⁸, etc. positively optimize carrier concentration by suppressing the Ge vacancies, but introducing exotic elements usually hampers the carrier transport. It is expected that inevitable vacancies may have less impact on carrier transport if they aggregate to form high-dimensional defects³⁹. Unlike point defects, these high-dimensional defects such as dislocations contribute to enhancing the phonon scattering without sacrificing the carrier mobility⁴⁰, thereby bringing opportunities to achieve enhanced thermoelectric performance by actively controlling Ge vacancies.

In this work, the defect structures of GeTe are engineered to optimize the carrier and phonon transport behaviors. This defect control strategy can be illustrated in the schematic diagram in Fig. 1a. The hierarchical structures from atomic-scale defects, nanoscale

dislocations, and domain structures with planar vacancies to mesoscale grain boundaries were established in GeTe. This type of engineered structure provides scattering sources at all relevant length scales, achieving an extremely low κ_L of $0.48 \text{ Wm}^{-1}\text{K}^{-1}$ close to the Cahill amorphous limit. The evolution of Ge vacancies also improves the carrier transport properties, increasing the weighted mobility μ_w (calculated from Supplementary Eq. S1) and the value of μ_w/κ_L (Fig. 1b). These great merits represent a higher quality factor B (calculated from Supplementary Eq. S2) for Ge-deficient samples sintered at 873 K (Fig. 1c), showing considerable potential as high ZT thermoelectric candidates. Finally, a peak ZT value of over 2.3 at 648 K and a ZT_{avg} value of 1.56 was achieved in the carrier concentration-optimized sample ($\text{Bi}_{0.07}\text{Ge}_{0.90}\text{Te}$) sintered at 873 K. By adopting the proposed strategy, the thermoelectric performance of GeTe compounds is significantly enhanced compared to the previously reported Bi-doped samples (without Ge deficiency), as shown in Supplementary Fig. 1. The present work illustrates the positive role of Ge vacancies in improving the thermoelectric performance of GeTe via rational manipulation.

Results and discussion

Vacancy manipulation in GeTe

According to the conventional view that Ge vacancies hinder the propagation of carriers, their excess is considered detrimental to the thermoelectric performance of GeTe. This negative effect was also discovered in the present work. It can be seen that the Hall mobility (μ_H) and μ_w are reduced by 54.9% and 26.1% in the $\text{Ge}_{0.97}\text{Te}$ sample sintered at 723 K (namely, $\text{Ge}_{0.97}\text{Te}$ -723), compared with the pristine GeTe sample (Table 1). By contrast, the κ_L only shows a 3.4% reduction at room temperature, meaning that a random distribution of Ge vacancies is not desirable for GeTe.

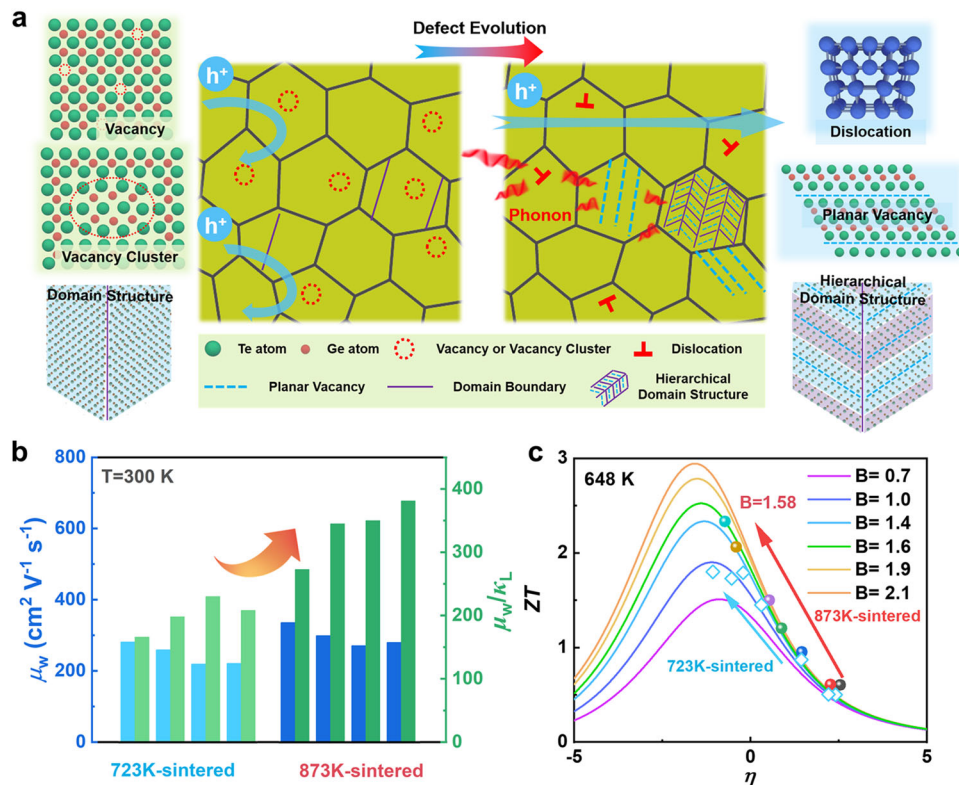


Fig. 1 | Synergistic control of the carrier and phonon transports via defect engineering. **a** The schematic diagram presenting the behaviors of carriers and phonons in the GeTe-based compounds with the presence of hierarchical structures. **b** The weighted mobility μ_w and the value of μ_w/κ_L of Ge-deficient samples

sintered at 873 K at the room temperature, as compared with samples sintered at 723 K. **c** ZT value as a function of reduced Fermi potential with different quality factors at 648 K.

Essentially, the randomly distributed vacancies enhance both the carrier and phonon scattering, but the former is, unfortunately, more intensified and not desired. Interestingly, the carrier scattering could be weakened with further enhanced phonon scattering when the Ge vacancies are actively controlled to form a hierarchical structure (the details are presented in the following section). This active control of Ge vacancies is achieved by simple but effective heat treatment at 873 K, which helps to redistribute the Ge vacancies. As shown in Table 1, higher μ_H and μ_w with a lower κ_L are achieved in the Ge_{0.97}Te sample sintered at 873 K (Ge_{0.97}Te-873) compared to the Ge_{0.97}Te-723 sample. The μ_w is increased by 19.6%, while the κ_L is decreased by 27.2%. Consequently, the value of μ_w/κ_L is increased dramatically, leading to a higher B and therefore higher thermoelectric potential in Ge-deficient samples.

Table 1 | Thermoelectric transport parameters at room temperature for the GeTe and Ge_{0.97}Te samples

Sample	σ	n_H	μ_H	μ_w	κ_L	μ_w/κ_L
GeTe-723	5.61	5.28	66.3	376	1.75	215
Ge _{0.97} Te-723	5.26	11.0	29.9	281	1.69	166
Ge _{0.97} Te-873	5.62	10.7	34.5	336	1.23	273

(Units: σ (10^3 S cm⁻¹), n_H (10^{20} cm⁻³), μ_H (cm² V⁻¹ s⁻¹), μ_w (cm² V⁻¹ s⁻¹), κ_L (W m⁻¹ K⁻¹), μ_w/κ_L (cm² V⁻¹ s⁻¹ / W m⁻¹ K⁻¹)).

Microstructural evolution via the active control of Ge vacancies
As discussed above, at the higher sintering temperature, the undesired excessive Ge vacancies in GeTe are conducive to enhancing the transport properties. In order to reveal the underlying mechanism of this unusual phenomenon, structure analysis was carried out as follows.

As for Ge_{0.97}Te-723, the domain structure in the submicron dimension is observed under a transmission electron microscope (TEM) (Fig. 2a and Supplementary Fig. 3a, b), together with a few dislocations and vacancy clusters inside some grains. As for the Ge-deficient samples sintered at 873 K, typical nanodomain structures and high-density dislocations are observed in a randomly selected area (Fig. 2b). The high-resolution TEM (HRTEM) image (Fig. 2c) illustrates the special hierarchical structure with submicron domains, nanodomains, and planar vacancies. Furthermore, dislocations and planar vacancies are also observed (Fig. 2e). The fast Fourier transformation (FFT) shows the special elongated diffraction spots of the planar vacancy (Fig. 2f). Figure 2g–i show the inverse FFT (IFFT) image (Fig. 2g) and strain mapping along the xx direction (Fig. 2h) and xy direction (Fig. 2i) from Fig. 2e, revealing the high-density dislocations and the large strain fluctuation induced by dislocations and planar vacancies. As a result of the high-temperature sintering process, the metastable state can be easily broken, facilitating the evolution of vacancies to higher-dimensional defects. In particular, the diffusion and accumulation of these positively charged Ge vacancies give rise to

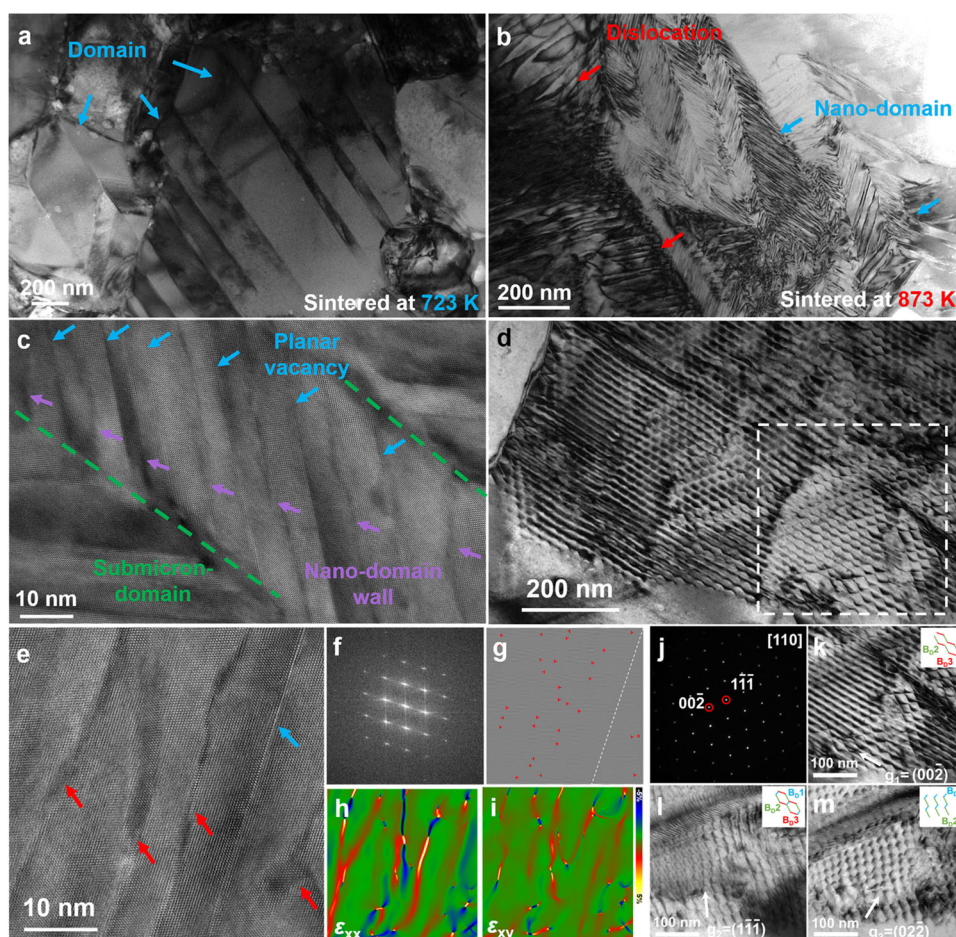


Fig. 2 | Microstructure evolution led by vacancies. **a, b** Low-magnification TEM images of the Ge-deficient samples sintered at 723 K and 873 K, respectively. **c** The HRTEM image of a randomly selected region in **b** showing the domain walls and planar vacancies in the sample sintered at 873 K. **d** Low-magnification TEM image of the dislocation network in the sample sintered at 873 K. **e** HRTEM image of

dislocations and planar vacancies. **f** The FFT image for **e**. **g** The IFFT images of **e**. Strain mapping along xx direction (**h**) and xy direction (**i**) confirmed by geometric phase analysis (GPA). **j** The selected area electron diffraction (SAED) of **d** marked with a white dashed square. The enlarged images of the framed area in **d** with three different diffraction conditions **k** $g = (00\bar{2})$, **l** $g = (1\bar{1}\bar{1})$, and **m** $g = (0\bar{2}\bar{2})$.

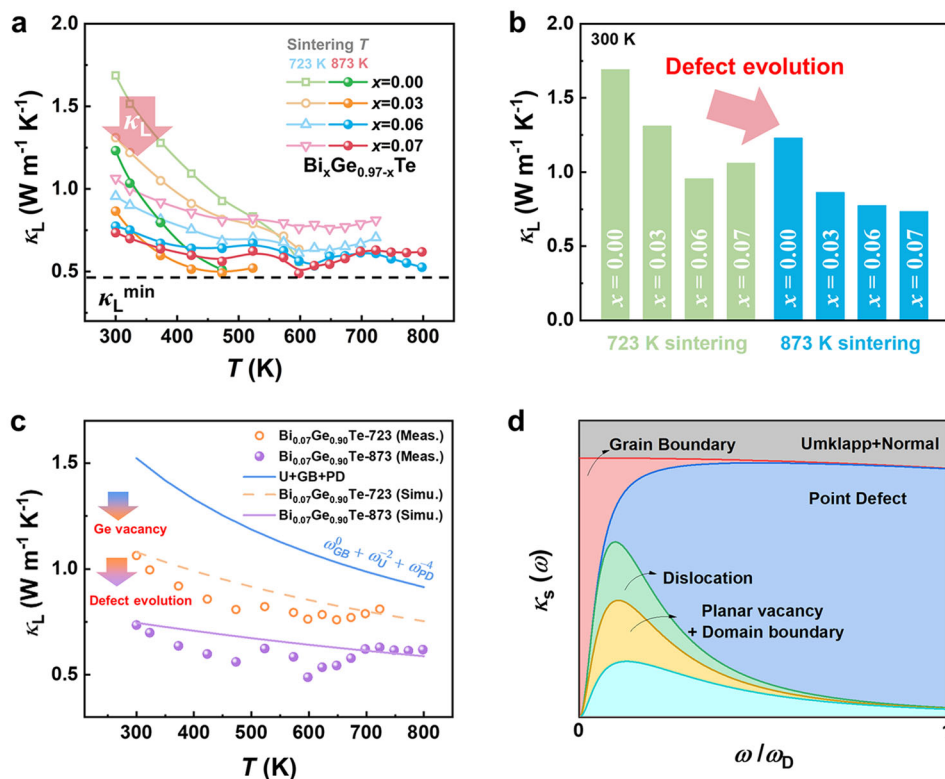


Fig. 3 | Lattice thermal conductivity and Debye-Callaway model prediction. **a** Temperature-dependent κ_L for the $\text{Bi}_x\text{Ge}_{0.97-x}\text{Te}$ -723 and $\text{Bi}_x\text{Ge}_{0.97-x}\text{Te}$ -873 samples, respectively. **b** The comparison of κ_L at room temperature for the $\text{Bi}_x\text{Ge}_{0.97-x}\text{Te}$ -723 and $\text{Bi}_x\text{Ge}_{0.97-x}\text{Te}$ -873 samples. **c** Temperature-dependent κ_L for the $\text{Bi}_{0.07}\text{Ge}_{0.90}\text{Te}$ -723 and $\text{Bi}_{0.07}\text{Ge}_{0.90}\text{Te}$ -873 samples (symbols). The lines showing

the prediction κ_L for $\text{Bi}_{0.07}\text{Ge}_{0.90}\text{Te}$ -723 and $\text{Bi}_{0.07}\text{Ge}_{0.90}\text{Te}$ -873 samples. **d** Calculated κ_S using the Debye-Callaway model with different scattering mechanisms including the Umklapp process scattering (U), grain boundary scattering (B), point defect scattering (PD), dislocation scattering (D), planar vacancy scattering (PV), domain boundary scattering (DB) at 300 K.

vacancy clusters and planar vacancies, where the negatively charged nanoscale domain walls can be attracted to balance the electric field, thereby promoting the formation of nanodomain structures^{15,41,42}. Additionally, the vacancy clusters can also collapse into closed loops of edge dislocations. The vacancy diffusion could facilitate dislocation migration, thereby increasing the dislocation density. According to our density functional theory (DFT) results of the present study (Supplementary Fig. 2), the formation energy of dislocations is negative, serving as evidence for the presence of abundant dislocations in the Ge-deficient samples. In addition, different sintering conditions (the sintering temperatures: 723 K, 773 K, 873 K, and 923 K) were applied, and the corresponding TEM characterization was displayed in Supplementary Figs. 3–6, which show the evolution of defect structures in detail. The phase characterization was shown in Supplementary Figs. 7–9 and Supplementary Tables 1–2.

Figure 2d displays a typical dislocation network, and the corresponding selected area electron diffraction pattern indicates fine crystals in Fig. 2j. Here, as the interaxial angle α is close to 90° (Supplementary Table 1), the same Burgers vector $\mathbf{B}_D = a/2[011]$ for the perfect dislocation in PbTe system¹⁰ is adopted. The detailed dislocation structure is also presented in Supplementary Fig. 5, where the white arrows follow a complete Burgers loop of the dislocation with the black arrow representing $\mathbf{B}_D = a/2[011]$. The IFFT images show the extra half-planes of the dislocation (Supplementary Fig. 5). The \mathbf{B}_D of the individual dislocations were determined by comparing two-beam diffraction contrast images using different diffraction vectors \mathbf{g} . Figure 2k–m shows the enlarged view of the white-circled area of Fig. 2d in different diffraction vectors \mathbf{g} of (002), (111), and (022), which were utilized to determine the \mathbf{B}_D of entire dislocations sets. As discussed above, GeTe consists of edge dislocations with $\mathbf{B}_D = a/2[110]$. The inset images in Fig. 2k–m display a hexagon formed by the Burgers

vectors of \mathbf{B}_{D1} , \mathbf{B}_{D2} , and \mathbf{B}_{D3} . According to the principle of minimum energy, the dislocation in one orientation can be easily merged by the other two orientations^{43,44}. As displayed in Supplementary Table 3, the Burgers vectors are $\mathbf{B}_{D1} \parallel a/2[110]$ or $a/2[\bar{1}\bar{1}0]$, $\mathbf{B}_{D2} \parallel a/2[10\bar{1}]$ or $a/2[011]$, and $\mathbf{B}_{D3} \parallel a/2[011]$. According to the dislocation reaction, the only solution is $a/2[10\bar{1}] + a/2[011] = a/2[110]$, where $\mathbf{B}_{D1} \parallel a/2[110]$, $\mathbf{B}_{D2} \parallel a/2[10\bar{1}]$, and $\mathbf{B}_{D3} \parallel a/2[011]$. This reaction satisfies the energy and geometry conditions. This type of network is made up of a large number of dislocations⁴⁵. By comparing the differences in microstructures among the samples sintered at 723 K, 773 K, 873 K, and 923 K, it is clear that the supersaturated vacancies' migration and accumulation at high temperatures is key to activating the microstructural evolution, as displayed in Fig. 1a. The abundant microstructures, stemming from Ge vacancies, are the main reason for the enhanced quality factor in the Ge-deficient samples sintered at 873 K, which will be investigated as follows.

Reduced lattice thermal conductivity via defect engineering

Due to the formation of hierarchical domain structures and high-density dislocations via the active control of Ge vacancies, κ_L sharply decreases by $\sim 27\%$ on average for the $\text{Bi}_x\text{Ge}_{0.97-x}\text{Te}$ -873 samples (Fig. 3a). Here, κ_e is calculated according to the Wiedemann-Franz law, and κ_L is obtained by subtracting κ_e from κ (displayed in Supplementary Fig. 10). The significantly reduced κ_L is related to the multiple defect structures and Bi doping, as shown in Fig. 3b. The chemical compositions for the $\text{Bi}_x\text{Ge}_{0.97-x}\text{Te}$ -873 samples are shown in Supplementary Table 4. Consequently, the minimum κ_L of $0.48 \text{ W m}^{-1} \text{ K}^{-1}$ is achieved in the $\text{Bi}_{0.07}\text{Ge}_{0.90}\text{Te}$ -873 sample, nearly approaching the theoretically minimum κ_L of GeTe following the Cahill model⁴⁶.

To further understand the roles of the hierarchical domain structure with planar vacancies and dense dislocations, the κ_L was

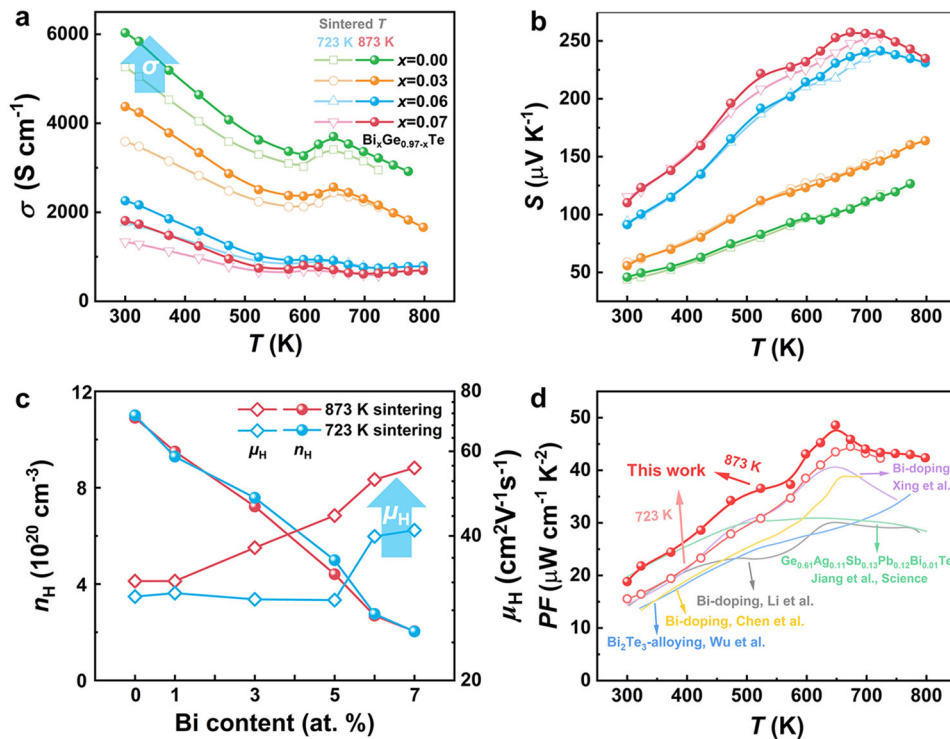


Fig. 4 | The electrical transport properties. Temperature-dependent **a** σ and **b** S for the $\text{Bi}_x\text{Ge}_{0.97-x}\text{Te}$ -723 and $\text{Bi}_x\text{Ge}_{0.97-x}\text{Te}$ -873 samples. **c** Hall carrier concentration and μ_{H} for the $\text{Bi}_x\text{Ge}_{0.97-x}\text{Te}$ -723 and $\text{Bi}_x\text{Ge}_{0.97-x}\text{Te}$ -873 samples at room

temperature. **d** Temperature-dependent PF for our samples compared to other literatures^{34,48–51}.

fitted by the Debye-Callaway model (shown in Supplementary Materials), which can provide useful insights into the phonon transport behavior. Here, κ_{L} can be calculated from the following equation⁴⁷:

$$\kappa_{\text{L}} = \frac{k_{\text{B}}}{2\pi^2 v_{\text{s}}} \left(\frac{k_{\text{B}} T}{\hbar} \right)^3 \int_0^{\theta_{\text{D}}} \tau_{\text{tot}} \frac{z^4 e^z}{(e^z - 1)^2} dz \quad (1)$$

The integrand item, in conjunction with the coefficient of Eq. 1, is the spectral lattice thermal conductivity (κ_{s}), namely:

$$\kappa_{\text{s}} = \frac{k_{\text{B}}}{2\pi^2 v_{\text{s}}} \left(\frac{k_{\text{B}} T}{\hbar} \right)^3 \tau_{\text{tot}} \frac{z^4 e^z}{(e^z - 1)^2} \quad (2)$$

where k_{B} is the Boltzmann constant, v_{s} is the average sound speed, \hbar is the reduced Planck constant, θ_{D} is the Debye temperature, $z = \hbar\omega/k_{\text{B}}T$ (ω denoting the phonon frequency) is the reduced phonon frequency and τ_{tot} is the total relaxation time, namely:

$$\tau_{\text{tot}}^{-1} = \tau_{\text{U}}^{-1} + \tau_{\text{B}}^{-1} + \tau_{\text{PD}}^{-1} + \tau_{\text{PV}}^{-1} + \tau_{\text{D}}^{-1} + \tau_{\text{DB}}^{-1} \quad (3)$$

The sound velocities (longitudinal, transverse, and average sound velocity) of the $\text{Bi}_x\text{Ge}_{0.97-x}\text{Te}$ -723 and $\text{Bi}_x\text{Ge}_{0.97-x}\text{Te}$ -873 samples were measured and are displayed in Supplementary Fig. 10. Other parameters are determined from earlier studies^{26,48}. More details about this model can be found in the Supplementary Materials.

As shown in Fig. 3c, κ_{L} is remarkably reduced via defect engineering in the $\text{Bi}_{0.07}\text{Ge}_{0.90}\text{Te}$ -873 sample. The solid blue line indicates the contribution from the Umklapp process scattering, the grain boundary scattering, and point defect scattering (Ge vacancies and Bi atoms). The orange line represents the contribution of a few dislocations and domain structures in phonon transport. Given the defect evolution process, the simulated decreased κ_{L} is displayed by the purple line. Notably, the simulated value is in good agreement with the experimental value. The comparison manifests the significant role of

dislocations and domain structures with planar vacancies via defect engineering in enhancing phonon scattering. The frequency-dependent accumulative reduction in κ_{L} is presented in Fig. 3d. Grain boundaries are responsible for scattering the low-frequency phonons, while point defects target the high-frequency phonons. By contrast, dislocations and planar vacancies effectively reduce κ_{L} by scattering the mid-frequency phonons in the mid-temperature range. Consequently, the phonon transport is suppressed by defect structure engineering via active control of Ge vacancies, and a low κ_{L} was achieved.

Electrical transport properties

The σ and S of the $\text{Bi}_x\text{Ge}_{0.97-x}\text{Te}$ -723 and $\text{Bi}_x\text{Ge}_{0.97-x}\text{Te}$ -873 samples are displayed in Fig. 4a, b. When subject to the higher sintering temperature, the σ shows a pronounced increase while S hardly changes, which deviates from the conventional compromising relationship between S and σ . Therefore, the Hall measurement was carried out and the results are shown in Fig. 4c; defect engineering does not modify the carrier concentration but improves the μ_{H} . The almost constant S is ascribed to the unchanged carrier concentration. At the same time, the increased electrical conductivity comes from the enhanced μ_{H} . The μ_{H} for $\text{Bi}_{0.07}\text{Ge}_{0.90}\text{Te}$ -873 reached $55.4 \text{ cm}^2 \text{ V}^{-1} \text{ s}^{-1}$, while a lower result of $41.1 \text{ cm}^2 \text{ V}^{-1} \text{ s}^{-1}$ was obtained for $\text{Bi}_{0.07}\text{Ge}_{0.90}\text{Te}$ -723. The extraordinarily increased μ_{H} after defect engineering indicates that the formation of hierarchical structures instead of high-concentration vacancies has less impact on electron transport, demonstrating that dislocations and planar vacancies are more favorable defects in thermoelectricity. The relationship between the carrier scattering and dislocations is described by $\mu_{\text{H}}^{-1} T^{3/2}$ ⁴⁰ also showing negligible effects of dislocations on the carrier transport (Supplementary Figs. 11–12). Consequently, the improved σ leads to the increased PF (shown in Supplementary Fig. 13); a high PF was obtained at 648 K via defect engineering, reaching $48 \mu\text{W cm}^{-1} \text{ K}^{-2}$ and $45 \mu\text{W cm}^{-1} \text{ K}^{-2}$ for $\text{Bi}_{0.06}\text{Ge}_{0.91}\text{Te}$ -873 and $\text{Bi}_{0.07}\text{Ge}_{0.90}\text{Te}$ -873, respectively. Compared with findings in the

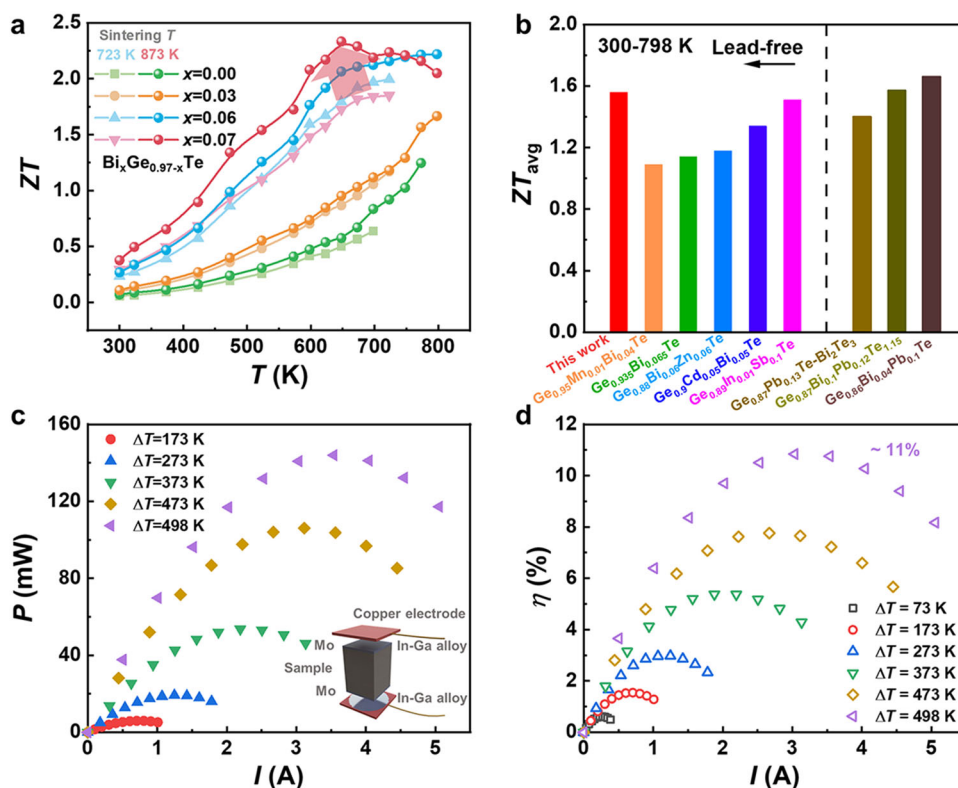


Fig. 5 | Thermoelectric properties and conversion efficiency. Temperature-dependent **a** figure of merit ZT for $\text{Bi}_x\text{Ge}_{0.97-x}\text{Te}$ -723 and $\text{Bi}_x\text{Ge}_{0.97-x}\text{Te}$ -873 samples and **b** the average ZT for the $\text{Bi}_{0.07}\text{Ge}_{0.90}\text{Te}$ -873 sample compared with the

previously reported typical GeTe-based materials^{18,22,26,34,50,60–62}. Current-dependent **c** output power and **d** efficiency of the single-leg GeTe thermoelectric device.

previous literatures^{34,48–51}, the sample in the present study displays a much higher PF in Bi-doped GeTe samples, verifying the validity of the proposed strategy in manipulating electrical transport properties. More details about the electrical transport properties are provided in Supplementary Tables 5–6.

The μ_w can be calculated from Supplementary Eq. S1⁵². The $\text{Bi}_x\text{Ge}_{0.97-x}\text{Te}$ -873 samples show much higher μ_w than the $\text{Bi}_x\text{Ge}_{0.97-x}\text{Te}$ -723 samples (Fig. 1 and Supplementary Tables 5–6), which also indicates that superior electrical transport properties can be achieved by actively controlling Ge vacancies. It is found that minimal Bi substitution (≤ 7 at.%) shows limited effects on μ_w . The mean free path lengths of phonons and carriers are summarized in Supplementary Table 7, where the shorter mean free path of phonons and longer mean free path of carriers are presented. Furthermore, the value of μ_w/κ_L for the $\text{Bi}_x\text{Ge}_{0.97-x}\text{Te}$ -873 samples is at a higher value (Supplementary Tables 5–6), manifesting a higher B , as shown in Fig. 1c.

ZT value and conversion efficiency

In the present work, the phonons are selectively scattered through the active control of defect structures, which breaks the long-standing bottleneck of defect engineering, leading to high mobility and PF . As a consequence, the thermoelectric performance is greatly improved. Figure 5a displays the temperature dependence of ZT . A maximum ZT of over 2.3 at 648 K is obtained in the $\text{Bi}_{0.07}\text{Ge}_{0.90}\text{Te}$ -873 sample, compared to the maximum ZT of 1.9 at 723 K for the $\text{Bi}_{0.07}\text{Ge}_{0.90}\text{Te}$ -723 sample. A high average ZT value of 1.56 was also achieved at the temperature range of 300 K to 798 K (Fig. 5b), which is comparable to that of the Pb-doped samples, and is also a record-high value in lead-free GeTe-based compounds. Our samples show good reproductivity during the cycling measurement (Supplementary Figs. 14–15). However, as for phonon transport properties, compared with the theoretical amorphous limit ($\approx 0.28 \text{ W m}^{-1}\text{K}^{-1}$ calculated by the diffusion model⁵³)

and the low κ_L reported for high-entropy GeTe samples⁵¹, the κ_L in the present work is at a modest level indicating that there is still scope for enhancing the thermoelectric performance of GeTe by optimizing κ_L .

A high theoretical conversion efficiency approaching 15% ($T_{\text{cold}} = 300$ K) was simulated for the single-leg thermoelectric $\text{Bi}_{0.07}\text{Ge}_{0.90}\text{Te}$ module at 798 K, as shown in Supplementary Fig. 16. The high output power of 144 mW with a power density of 1.82 W cm^{-2} was obtained at a temperature difference (ΔT) of 498 K (Fig. 5c). The high output power and power density are strongly correlated with the high PF at elevated temperatures. However, during the efficiency test at an elevated temperature using the mini-PEM module testing system, thermal radiation significantly impacted on the test of the heat flow Q_c , which is difficult to be measured accurately. Hence, the heat flow through the device was overestimated^{54,55}. The heat flow was calibrated with the simulated Q_c data in Fig. 5d, leading to energy conversion efficiency up to 11% at $\Delta T = 498$ K.

In summary, this study reveals that defect evolution can be induced by actively controlling the Ge vacancies in GeTe-based compounds to form high-dimensional defects, which favors the phonon scattering without affecting the carrier transport. Controlling Ge vacancies is achieved by the high-temperature heat treatment, which promotes the transformation of supersaturated vacancies, giving rise to dense dislocations and dislocation networks. Meanwhile, the positively charged Ge vacancies can be attracted by the negatively charged nanoscale domain walls, which induces hierarchical nanodomain structures with planar vacancies, further strengthening the scattering of the mid-frequency phonons. More prominently, higher carrier mobility demonstrates the effective role of such a defect structure in breaking the conventional relationship of S and σ . As a result, the $\text{Bi}_{0.07}\text{Ge}_{0.90}\text{Te}$ -873 sample holds a maximum PF of $45 \mu \text{ W cm}^{-1}\text{K}^{-2}$ at 648 K and a minimum κ_L of $0.48 \text{ W m}^{-1}\text{K}^{-1}$. A peak ZT value over 2.3 at 648 K and a high average ZT of 1.56 within the range of 300–798 K are

achieved. The thermoelectric energy conversion efficiency of a single-leg $\text{Bi}_{0.07}\text{Ge}_{0.90}\text{Te}$ module reaches up to 11% at $\Delta T = 498$ K. This study demonstrates that defect structure engineering through actively controlling the Ge vacancies is a simple and effective approach for fabricating high-performance GeTe-based materials, qualifying them to be promising lead-free candidate compounds at mid-temperature range.

Methods

Synthesis

Raw materials, germanium (granules, 2–5 mm, 99.999%), tellurium (powder, 99.999%), and bismuth (powder, 99.99%) were weighed in the glove box and loaded into tungsten carbide jars according to the stoichiometric ratios of $\text{Bi}_x\text{Ge}_{0.97-x}\text{Te}$ ($x = 0, 0.03, 0.06, 0.07$). First, the mixture was reacted via mechanical alloying in a planetary ball mill at 460 rpm for 12 h, with argon (>99.5%) as the protective gas. Then, the obtained powders were densified by spark plasma sintering (SPS 211Lx, Fuji Electronic, Japan) at 723 K, 773 K, 873 K, or 923 K for 5 min under a pressure of 60 MPa.

Characterization

The phase purity of samples was identified by X-ray diffraction (XRD, D8 ADVANCE, Bruker, Germany, $\text{Cu K}\alpha$, $\lambda = 1.5418$ Å). The grain morphology and microstructure were investigated by field-emission scanning electron microscopy (Zeiss Merlin, Germany), and transmission electron microscopy (TEM, 2100 F, JEOL, Japan). The elemental distribution was studied via electronic probe microscopic analysis (JXA-8230, JEOL, Japan).

Transport properties measurement

S and σ were measured by the measuring system (ZEM-3, ADVANCE RIKO, Inc., Japan) in helium atmosphere. The bulk samples were cut and polished into bars with dimensions of $2.5 \text{ mm} \times 2.5 \text{ mm} \times 9 \text{ mm}$ and disks of $\varnothing 6 \text{ mm} \times 1 \text{ mm}$. The disks were used for thermal diffusion coefficient (D) measurements using the laser flash method (LFA457, Netzsch, Germany). The thermal conductivity was calculated from the equation $\kappa = DC_p \rho$, where C_p is the specific heat deduced via the Dulong–Petit limit, and d is the density measured by Archimedes' method. The electrical thermal conductivity was calculated using the Wiedemann–Franz law $\kappa_e = \sigma LT$, where the Lorenz factor (L) was estimated by the single parabolic band model. The lattice thermal conductivity was obtained by subtracting κ_e from κ . The electrical and thermal transport properties were measured perpendicular to the axial SPS pressure. The pieces of $10 \text{ mm} \times 10 \text{ mm} \times 0.5 \text{ mm}$ were used for Hall coefficient (R_H) measurements under a reversible magnetic field of 0.52 T (ResiTest 8340DC, Tokyo, Japan). The Hall carrier concentration (n_H) and mobility (μ_H) were calculated using $n_H = 1/(eR_H)$ and $\mu_H = \sigma R_H$, respectively. The sound velocity (v) was measured by the ultrasonic pulse-echo technique (5072PR, Olympus, Tokyo, Japan).

The fabrication and characterization of the thermoelectric device

The thermoelectric single-leg module was assembled by SPS at 873 K for 30 min under a pressure of 60 MPa. It was then cut into a block with the size of $2.8 \text{ mm} \times 2.8 \text{ mm} \times 6 \text{ mm}$ with Mo/In-Ga alloy as the contact layer. The energy conversion efficiency (η) of the single-leg device was calculated using the equation $\eta = P/Q \times 100\%$, where the output power (P) and heat flow per unit time (Q) were simultaneously measured via the Mini-PEM testing system (ADVANCE RIKO, Inc., Japan). The theoretical conversion efficiency and heat flow of the single-leg module was simulated via COMSOL Multiphysics software.

The DFT calculation

An ab-initio MD simulation for GeTe was performed by the Vienna ab-initio Simulation Package^{56–58} in a canonical ensemble (NVT

ensemble) using the Nose-Hoover thermostat at 300 K. The projector augmented wave potentials are used to describe the interaction between electrons and ions. Generalized gradient approximation in the scheme of Perdew–Burke–Ernzerhof⁵⁹ is employed to describe the exchange and correlation function. The cutoff energy was set to 400 eV, and the total energy converged to 1.0×10^{-5} eV per atom. A typical edge dislocation in GeTe rhombohedral phase with R3m space group was simulated using a supercell containing 285 atoms. The dislocation formation energy was calculated using the following equation: $E_f = (E_{\text{tot}} - \sum n_\alpha E_\alpha) / \sum n_\alpha$ ¹⁰, where E_{tot} represents the total energy of the system, n_α denotes the number of α atoms, and E_α is the total energy of an α atom in its ground-state bulk phase.

Reporting summary

Further information on research design is available in the Nature Research Reporting Summary linked to this article.

Data availability

The data that support the findings of this study are available from the corresponding author on request.

References

- He, J. & Tritt, T. M. Advances in thermoelectric materials research: looking back and moving forward. *Science* **357**, eaak9997 (2017).
- Petsagkourakis, I. et al. Thermoelectric materials and applications for energy harvesting power generation. *Sci. Technol. Adv. Mat.* **19**, 836–862 (2018).
- Kraemer, D. et al. High-performance flat-panel solar thermoelectric generators with high thermal concentration. *Nat. Mater.* **10**, 532–538 (2011).
- Ding, T. et al. Scalable thermoelectric fibers for multifunctional textile-electronics. *Nat. Commun.* **11**, 6006 (2020).
- Pei, Y. et al. Convergence of electronic bands for high performance bulk thermoelectrics. *Nature* **473**, 66–69 (2011).
- Li, A. et al. Demonstration of valley anisotropy utilized to enhance the thermoelectric power factor. *Nat. Commun.* **12**, 5408 (2021).
- Biswas, K. et al. High-performance bulk thermoelectrics with all-scale hierarchical architectures. *Nature* **489**, 414–418 (2012).
- Kim, S. I. et al. Dense dislocation arrays embedded in grain boundaries for high-performance bulk thermoelectrics. *Science* **348**, 109–114 (2015).
- Heremans, J. P. et al. Enhancement of thermoelectric efficiency in PbTe by distortion of the electronic density of states. *Science* **321**, 554–557 (2008).
- Wu, Y. et al. Lattice strain advances thermoelectrics. *Joule* **3**, 1276–1288 (2019).
- Zhao, L.-D. et al. Ultralow thermal conductivity and high thermoelectric figure of merit in SnSe crystals. *Nature* **508**, 373–377 (2014).
- Zhou, C. et al. Polycrystalline SnSe with a thermoelectric figure of merit greater than the single crystal. *Nat. Mater.* **20**, 1378–1384 (2021).
- Liu, H. et al. Copper ion liquid-like thermoelectrics. *Nat. Mater.* **11**, 422–425 (2012).
- Lee, H. S. et al. Herringbone structure in GeTe-based thermoelectric materials. *Acta Mater.* **91**, 83–90 (2015).
- Wu, D., Xie, L., Xu, X. & He, J. High thermoelectric performance achieved in GeTe– Bi_2Te_3 pseudo-binary via van der Waals gap-induced hierarchical ferroelectric domain structure. *Adv. Funct. Mater.* **29**, 1806613 (2019).
- Zhang, X. et al. GeTe thermoelectrics. *Joule* **4**, 986–1003 (2020).
- Liu, W. et al. High-performance GeTe-based thermoelectrics: from materials to devices. *Adv. Energy Mater.* **10**, 2000367 (2020).
- Feng, Y. et al. Band convergence and carrier-density fine-tuning as the electronic origin of high-average thermoelectric performance

- in Pb-doped GeTe-based alloys. *J. Mater. Chem. A* **8**, 11370–11380 (2020).
19. Gelbstein, Y., Davidow, J., Girard, S. N., Chung, D. Y. & Kanatzidis, M. Controlling metallurgical phase separation reactions of the $\text{Ge}_{0.87}\text{Pb}_{0.13}\text{Te}$ alloy for high thermoelectric performance. *Adv. Energy Mater.* **3**, 815–820 (2013).
20. Nshimiyimana, E. et al. Discordant nature of Cd in GeTe enhances phonon scattering and improves band convergence for high thermoelectric performance. *J. Mater. Chem. A* **8**, 1193–1204 (2020).
21. Wu, L. et al. Resonant level-induced high thermoelectric response in indium-doped GeTe. *NPG Asia Mater.* **9**, e343–e343 (2017).
22. Hong, M. et al. Realizing zT of 2.3 in $\text{Ge}_{1-x-y}\text{Sb}_x\text{In}_y\text{Te}$ via reducing the phase-transition temperature and introducing resonant energy doping. *Adv. Mater.* **30**, 1705942 (2018).
23. Shuai, J. et al. Enhanced thermoelectric performance through crystal field engineering in transition metal-doped GeTe. *Mater. Today Phys.* **9**, 100094 (2019).
24. Zhang, R. et al. Intrinsic vacancy suppression and band convergence to enhance thermoelectric performance of (Ge, Bi, Sb)Te crystals. *Chem. Eng. J.* **429**, 132275 (2022).
25. Li, Y., Chen, J., Cai, P. & Wen, Z. An electrochemically neutralized energy-assisted low-cost acid-alkaline electrolyzer for energy-saving electrolysis hydrogen generation. *J. Mater. Chem. A* **6**, 4948–4954 (2018).
26. Hong, M. et al. Arrays of planar vacancies in superior thermoelectric $\text{Ge}_{1-x-y}\text{Cd}_x\text{Bi}_y\text{Te}$ with band convergence. *Adv. Energy Mater.* **8**, 1801837 (2018).
27. Xie, L. et al. Enhanced thermoelectric performance in $\text{Ge}_{0.955-x}\text{Sb}_x\text{Te}/\text{FeGe}_2$ composites enabled by hierarchical defects. *Small* **17**, 2100915 (2021).
28. Shuai, J., Sun, Y., Tan, X. & Mori, T. Manipulating the Ge vacancies and Ge precipitates through Cr doping for realizing the high-performance GeTe thermoelectric material. *Small* **16**, 1906921 (2020).
29. Dong, J. et al. Medium-temperature thermoelectric GeTe: vacancy suppression and band structure engineering leading to high performance. *Energy Environ. Sci.* **12**, 1396–1403 (2019).
30. Bu, Z. et al. Realizing a 14% single-leg thermoelectric efficiency in GeTe alloys. *Sci. Adv.* **7**, eabf2738 (2021).
31. Liu, Z. et al. High power factor and enhanced thermoelectric performance in Sc and Bi codoped GeTe: insights into the hidden role of rhombohedral distortion degree. *Adv. Energy Mater.* **10**, 2002588 (2020).
32. Yin, L.-C. et al. High carrier mobility and high figure of merit in the CuBiSe_2 alloyed GeTe. *Adv. Energy Mater.* **11**, 2102913 (2021).
33. Zhang, X. et al. Vacancy manipulation for thermoelectric enhancements in GeTe alloys. *J. Am. Chem. Soc.* **140**, 15883–15888 (2018).
34. Li, J. et al. Electronic origin of the high thermoelectric performance of GeTe among the p-type group IV monotellurides. *NPG Asia Mater.* **9**, e353–e353 (2017).
35. Bu, Z. et al. Dilute Cu_2Te -alloying enables extraordinary performance of r-GeTe thermoelectrics. *Mater. Today Phys.* **9**, 100096 (2019).
36. Perumal, S., Roychowdhury, S., Negi, D. S., Datta, R. & Biswas, K. High thermoelectric performance and enhanced mechanical stability of p-type $\text{Ge}_{1-x}\text{Sb}_x\text{Te}$. *Chem. Mater.* **27**, 7171–7178 (2015).
37. Li, J., Zhang, X., Lin, S., Chen, Z. & Pei, Y. Realizing the high thermoelectric performance of GeTe by Sb-doping and Se-alloying. *Chem. Mater.* **29**, 605–611 (2017).
38. Li, J. et al. Simultaneous optimization of carrier concentration and alloy scattering for ultrahigh performance GeTe thermoelectrics. *Adv. Sci.* **4**, 1700341 (2017).
39. Chen, Z. et al. Vacancy-induced dislocations within grains for high-performance PbSe thermoelectrics. *Nat. Commun.* **8**, 13828 (2017).
40. Choi, H. W., Zhang, J. & Chua, S. J. Dislocation scattering in n-GaN. *Mat. Sci. Semicon. Proc.* **4**, 567–570 (2001).
41. Chen, S. et al. The role of Ge vacancies and Sb doping in GeTe: a comparative study of thermoelectric transport properties in $\text{Sb}_x\text{Ge}_{1-1.5x}\text{Te}$ and $\text{Sb}_x\text{Ge}_{1-x}\text{Te}$ compounds. *Mater. Today Phys.* **24**, 100682 (2022).
42. Chen, S. et al. Vacancy-based defect regulation for high thermoelectric performance in $\text{Ge}_9\text{Sb}_2\text{Te}_{12-x}$ compounds. *ACS Appl. Mater. Interfaces* **12**, 19664–19673 (2020).
43. Wei, Y. L. et al. Dislocations, boundaries and slip systems in cube grains of rolled aluminium. *Scr. Mater.* **65**, 355–358 (2011).
44. McCabe, R. J., Misra, A. & Mitchell, T. E. Experimentally determined content of a geometrically necessary dislocation boundary in copper. *Acta Mater.* **52**, 705–714 (2004).
45. Abdellaoui, L. et al. Parallel dislocation networks and cottrell atmospheres reduce thermal conductivity of PbTe thermoelectrics. *Adv. Funct. Mater.* **31**, 2101214 (2021).
46. Cahill, D. G., Watson, S. K. & Pohl, R. O. Lower limit to the thermal conductivity of disordered crystals. *Phys. Rev. B* **46**, 6131–6140 (1992).
47. Callaway, J. & von Baeyer, H. C. Effect of point imperfections on lattice thermal conductivity. *Phys. Rev.* **120**, 1149–1154 (1960).
48. Xing, T. et al. Ultralow lattice thermal conductivity and superhigh thermoelectric figure-of-merit in (Mg, Bi) co-doped GeTe. *Adv. Mater.* **33**, 2008773 (2021).
49. Chen, B.-C., Wang, K.-K. & Wu, H.-J. Localized crystal imperfections coupled with phase diagram engineering yield high-performance rhombohedral GeTe thermoelectrics. *Mater. Today Phys.* **22**, 100617 (2022).
50. Wu, D. et al. Origin of the high performance in GeTe-based thermoelectric materials upon Bi_2Te_3 doping. *J. Am. Chem. Soc.* **136**, 11412–11419 (2014).
51. Jiang, B. et al. High figure-of-merit and power generation in high-entropy GeTe-based thermoelectrics. *Science* **377**, 208–213 (2022).
52. Snyder, G. J. et al. Weighted Mobility. *Adv. Mater.* **32**, 2001537 (2020).
53. Agne, M. T., Hanus, R. & Snyder, G. J. Minimum thermal conductivity in the context of diffusion-mediated thermal transport. *Energy Environ. Sci.* **11**, 609–616 (2018).
54. Chetty, R. et al. Power generation from the $\text{Cu}_{26}\text{Nb}_2\text{Ge}_6\text{S}_{32}$ -based single thermoelectric element with Au diffusion barrier. *J. Mater. Chem. C* **7**, 5184–5192 (2019).
55. Roychowdhury, S. et al. Enhanced atomic ordering leads to high thermoelectric performance in AgSbTe_2 . *Science* **371**, 722–727 (2021).
56. Kresse, G. & Hafner, J. Ab initio molecular dynamics for open-shell transition metals. *Phys. Rev. B* **48**, 13115–13118 (1993).
57. Kresse, G. & Furthmüller, J. Efficient iterative schemes for ab initio total-energy calculations using a plane-wave basis set. *Phys. Rev. B* **54**, 11169–11186 (1996).
58. Kresse, G. & Joubert, D. From ultrasoft pseudopotentials to the projector augmented-wave method. *Phys. Rev. B* **59**, 1758–1775 (1999).
59. Perdew, J. P., Burke, K. & Ernzerhof, M. Generalized gradient approximation made simple. *Phys. Rev. Lett.* **77**, 3865–3868 (1996).
60. Liu, Z. et al. Phase-transition temperature suppression to achieve cubic GeTe and high thermoelectric performance by Bi and Mn codoping. *Proc. Natl Acad. Sci. USA* **115**, 5332–5337 (2018).
61. Guo, Z. et al. Bi–Zn codoping in GeTe synergistically enhances band convergence and phonon scattering for high thermoelectric performance. *J. Mater. Chem. A* **8**, 21642–21648 (2020).
62. Li, J. et al. Low-symmetry rhombohedral GeTe thermoelectrics. *Joule* **2**, 976–987 (2018).

Acknowledgements

J.F.L., Y.L.J., J.F.D., H.L.Z., J.C.Y., B.S., J.P., F.H.S., M.Z., H.H.H., J.W.L., Z.R.H., and B.P.Z. acknowledge the Basic Science Center Project of NSFC no. 51788104 and the National Key R&D Program of China no. 2018YFB0703603. T.M. and H.Z.L. acknowledge support from JST Mirai JPMJMI19A1.

Author contributions

J.F.L. and Y.L.J. designed this work. Y.L.J., J.F.D., H.L.Z., J.C.Y., and B.S. synthesized the samples and carried out the transport property measurements. Y.L.J. and J.C.Y. analyzed the XRD results and carried out Rietveld refinement. Y.L.J., J.F.D., H.L.Z., and B.S. performed the TEM observations. Y.L.J., J.F.L., J.P., H.H.H., J.W.L., and Z.R.H. discussed the formation mechanisms. J.P. and B.P.Z. contributed to the DFT calculations. J.F.L., Y.L.J., J.C.Y., H.Z.L., F.H.S., M.Z., and B.S. analyzed the thermoelectric properties. Y.L.J. and J.F.L. wrote the manuscript. J.F.L., Y.L.J., J.F.D., M.Z., T.M., H.Z.L., and B.S. edited the manuscript.

Competing interests

The authors declare no competing interests.

Additional information

Supplementary information The online version contains supplementary material available at <https://doi.org/10.1038/s41467-022-33774-z>.

Correspondence and requests for materials should be addressed to Bin Su, Min Zhou, Takao Mori or Jing-Feng Li.

Peer review information *Nature Communications* thanks Iris Nandhakumar, Pengfei Qiu and the other anonymous reviewer(s) for their contribution to the peer review of this work.

Reprints and permission information is available at <http://www.nature.com/reprints>

Publisher's note Springer Nature remains neutral with regard to jurisdictional claims in published maps and institutional affiliations.

Open Access This article is licensed under a Creative Commons Attribution 4.0 International License, which permits use, sharing, adaptation, distribution and reproduction in any medium or format, as long as you give appropriate credit to the original author(s) and the source, provide a link to the Creative Commons license, and indicate if changes were made. The images or other third party material in this article are included in the article's Creative Commons license, unless indicated otherwise in a credit line to the material. If material is not included in the article's Creative Commons license and your intended use is not permitted by statutory regulation or exceeds the permitted use, you will need to obtain permission directly from the copyright holder. To view a copy of this license, visit <http://creativecommons.org/licenses/by/4.0/>.

© The Author(s) 2022